# Quantum Simulation of Ligand-like Molecules through Sample-based Quantum Diagonalization in Density Matrix Embedding Framework

Ashish Kumar Patra<sup>1</sup>, Anurag K. S. V.<sup>1</sup>, Sai Shankar P.<sup>1</sup>, Ruchika Bhat<sup>1, 2</sup>, Raghavendra V.<sup>3</sup>, Rahul Maitra<sup>4</sup>, and Jaiganesh G.\*, <sup>1</sup>

## **ABSTRACT**

The accurate treatment of electron correlation in extended molecular systems remains computationally challenging using classical electronic structure methods. Hybrid quantum—classical algorithms offer a potential route to overcome these limitations; however, their practical deployment on existing quantum computers requires strategies that both reduce problem size and mitigate hardware noise. In this work, we combine Density Matrix Embedding Theory (DMET) with Sample-based Quantum Diagonalization (SQD) to compute ground-state energies of a set of natural ligand-like molecules in the minimal Slater Type Orbital (STO-3G) basis set. DMET provides a systematic fragmentation of a molecule into embedded impurity subproblems, while SQD enables construction and classical diagonalization of reduced configuration spaces through quantum sampling enhanced by iterative configuration recovery. The resulting embedded Hamiltonians are solved on IBM's Eagle R3 superconducting quantum hardware (IBM Sherbrooke). The DMET-SQD energies obtained for all systems considered exhibit strong agreement with DMET-FCI benchmark values within chemical accuracy (1 kcal/mol). These results demonstrate that sample-based quantum methods, when integrated with a robust embedding framework, can reliably extend quantum computation towards simulation of chemically relevant molecular systems, showcasing potential applications in the field of drug discovery.

 $\textbf{Keywords:} \ \ Quantum \ \ Computing \cdot Quantum \ \ Simulation \cdot Quantum \ \ Chemistry \cdot Sample-based \ \ Algorithms \cdot Embedding \ \ Methods \cdot Hybrid \ \ Quantum-Classical \ \ Algorithms$ 

#### 1 Introduction

In quantum chemistry, the accurate simulation of many-electron systems remains a central goal. However, the increasing complexity of molecular systems renders such endeavours computationally demanding, often necessitating varying levels of approximation<sup>1</sup>. Current classical computational resources are insufficient to fully capture electron correlation in larger molecular systems, such as proteins. For instance, one of the largest Full Configuration Interaction (FCI) simulations carried out using classical methods involved propane ( $C_3H_8$ ), requiring the diagonalization of a Hilbert space spanning approximately  $1.31 \times 10^{12}$  determinants<sup>2</sup>, even when employing a minimal STO-3G basis set<sup>3</sup>. In quantum chemistry, Hartree-Fock (HF) theory continues to serve as the foundational approximation for all subsequent methods<sup>4</sup>.

With the advent of quantum computers, the accurate simulation of chemically and biologically relevant systems are expected to become increasingly tractable. Quantum algorithms promise the capability to model and evaluate protein-ligand interactions<sup>5–7</sup> and binding energetics, explore conformational landscapes of flexible bio-molecules<sup>8–14</sup>-tasks that rapidly become intractable on classical computers<sup>15</sup>. This has motivated increasing interest in quantum computing, which offers alternative algorithmic frameworks capable of addressing many-electron correlations more efficiently<sup>16,17</sup>.

Fault-tolerant Application-Scale Quantum (FASQ)<sup>18</sup> algorithms, such as Quantum Phase Estimation (QPE)<sup>19</sup> and Quantum Singular Value Transformation (QSVT)<sup>20</sup>, face significant challenges due to their requirement for deep quantum circuits, which remain impractical on current Noisy Intermediate-Scale Quantum (NISQ) hardware<sup>21</sup>. To facilitate execution on near-term devices, variational approaches such as the Variational Quantum Eigensolver (VQE)<sup>22</sup> were proposed. VQE evaluates the expectation value of the Hamiltonian directly through a hybrid classical–quantum optimization loop, iteratively improving

<sup>&</sup>lt;sup>1</sup>Qclairvoyance Quantum Labs, Secunderabad, TG 500094, India.

<sup>&</sup>lt;sup>2</sup>The University of Arizona, Tucson, AZ 85721, USA.

<sup>&</sup>lt;sup>3</sup>SRM Institute of Science and Technology, Chennai, TN 603203, India.

<sup>&</sup>lt;sup>4</sup>Indian Institute of Technology Bombay, Mumbai, MH 400076, India.

 $<sup>*(</sup>Corresponding\ Author)\ email:\ jaiganesh@qclairvoyance.in,\ drjaiganesh15@gmail.com$ 

the overlap between the parametrized quantum state and the true ground state. Recent developments<sup>23</sup> have produced more hardware-efficient variants, yet key limitations persist, including statistical fluctuations and physical noise inherent to NISQ devices, as well as the requirement for prohibitively large numbers of samples and extensive error mitigation strategies<sup>24</sup>.

Early hardware demonstrations of molecular problems using VQE, such as protein-ligand interactions, have been limited to active spaces involving around four qubits<sup>5</sup>, primarily restricted to small organic systems. To overcome these limitations, sample-based approaches such as Sample-Based Quantum Diagonalization (SQD)<sup>25</sup> have emerged. SQD integrates Quantum Selected Configuration Interaction (QSCI)<sup>26</sup> with an error-mitigation scheme known as Iterative Self-Consistent Configuration Recovery (S-CoRe)<sup>25</sup> and employs classical Selected Configuration Interaction (SCI)<sup>27</sup> for post-processing diagonalization. These methods have enabled the quantum sampling of molecules with up to 36 spatial orbitals, including the [4Fe-4S] complex in a 77-qubit experiment, using 6400 nodes of the *Fugaku* super-computer<sup>25</sup>.

While quantum computers are anticipated to handle strongly correlated systems more effectively-providing a compelling rationale for their adoption, counterarguments emphasize potential limitations<sup>28</sup>. Nonetheless, within the emerging paradigm of Quantum-Centric Super-Computing (QCSC)<sup>25</sup>, where classical supercomputers are coupled with quantum computers in a hybrid framework, SQD has facilitated a series of further algorithmic advancements.

Recent developments in sample-based quantum algorithms include applications to materials simulation<sup>29</sup>, excited-state energy estimation<sup>30</sup>, hybrid methods combining SQD with Krylov Subspace Diagonalization<sup>31</sup> and QDrift<sup>32</sup>, leading to techniques such as Sample-based Krylov Quantum Diagonalization(SKQD)<sup>33</sup> and SqDRIFT<sup>34</sup>. Additionally, methods like Handover Iterative VQE (HI-VQE)<sup>35</sup> have been developed to iteratively expand the configuration space, achieving chemical accuracy while sampling only a fraction of the symmetry space<sup>35</sup>, that is, configurations obeying number and spin symmetries.

In an earlier work, SQD was combined with the classical fragmentation technique, Density Matrix Embedding Theory (DMET)<sup>36</sup> and used to estimate the energies of extended molecules by Shajan et al.,<sup>12</sup>. For this study, we consider the following ligand-like molecules: Cyanic Acid (HOCN), Formaldehyde Oxime ( $CH_3NO$ ), O-methyl-hydroxylamine ( $CH_5NO$ ), Methyl Isocyanate ( $C_2H_3NO$ ), Acetaldehyde Oxime ( $C_2H_5NO$ ), Carbamide/Urea ( $CH_4N_2O$ ), Nitrosyl Chloride (NOCl), and Hydroxythiocyanate (HOSCN). All of these compounds have molecular weights below 76 Da (see Fig. 4) and together span a chemically diverse set of small, pharmacologically motivated molecular fragments. Several members of this set, particularly urea derivatives and methoxyamine-related fragments have established relevance in medicinal chemistry<sup>37–40</sup>. This diversity makes the collection an appropriate testbed for assessing sample-based quantum simulation techniques in the context of drug-discovery-oriented molecular systems.

Concisely detailing the work, in **Section 2** an overview of the methods used are described briefly, in **Section 3** the experimental details and methodology are discussed, in **Section 4** the results obtained are discussed and finally in **Section 5** we conclude the work and mention future prospects.

## 2 Theoretical Background

#### 2.1 Hamiltonian formulation

The first quantized Hamiltonian after the Born-Oppenheimer approximation<sup>41</sup> (excluding the nuclei-nuclei interactions, and kinetic energy terms of nuclei) is:

$$\hat{H}_{fq} = -\frac{\hbar^2}{2m_e} \sum_{i} \hat{\nabla}_{i}^{2} + \sum_{i}^{N} \sum_{j < i}^{N} \frac{e^2}{|\vec{r}_{i} - \vec{r}_{j}|} + \sum_{i}^{N} \sum_{A}^{M} \frac{Z_A \cdot e^2}{|\vec{r}_{i} - \vec{R}_A|}$$
(1)

where N is the number of electrons, M is the number of nuclei, e is the charge of an electron,  $Z_A$  is the charge of the  $A^{th}$  nucleus.  $\hbar = \frac{h}{2\pi}$ , h is Planck's constant  $(6.626 \times 10^{-34} \, m^2 \cdot kg \cdot s^{-1})$ . The vector  $\vec{r}_i(\vec{r}_j)$  denotes the displacement of the  $i^{th}(j^{th})$  electron from the origin, and the vector  $\vec{R}_A$  denotes the displacement of the  $A^{th}$  proton from the origin.

In second quantized form, the Hamiltonian is represented in the following manner:

$$\hat{H}_{sq} = \sum_{i,j} h_{ij} \hat{a}_i^{\dagger} \hat{a}_j + \sum_{p,q,r,s} h_{pqrs} \hat{a}_p^{\dagger} \hat{a}_q^{\dagger} \hat{a}_r \hat{a}_s \tag{2}$$

where  $\hat{a}_i^{\dagger}$  and  $\hat{a}_j$  represent the creation and annihilation operators<sup>42</sup> acting on the  $i^{th}$  and  $j^{th}$  spin-orbitals respectively. In quantum simulation algorithms, it is advantageous to initialize the quantum processor in a state that is both straightforward to prepare and exhibits substantial overlap with the true ground state. In our case, we initialize the quantum state in the HF computational basis state, which is a single Slater Determinant, as in this work, we confine ourselves to single-reference Restricted HF Theory. The initial state, hence, can be given in the following manner:

$$|\psi\rangle_{HF} = \prod_{i \in occ} a_i^{\dagger} |\emptyset\rangle \tag{3}$$

where  $|\emptyset\rangle$  represents total vacuum, and *occ* represents the occupied spin orbitals. Under the Jordan–Wigner transformation<sup>43</sup>, the corresponding occupation-number basis states map directly onto the computational (or measurable) basis states of the qubits in a universal gate-based quantum computer.

### 2.2 Local Unitary Cluster Jastrow Ansatz

We use the Local Unitary Cluster Jastrow (LUCJ)<sup>44</sup> ansatz, owing to it's chemistry informed nature and flexibility with different hardware topologies. The ansatz parameters are initialized with the single and double excitation parameters obtained using Coupled Cluster Singles and Doubles (CCSD)<sup>45</sup> parameters.

In Coupled Cluster, corrections of a specific type are added upto infinite order<sup>45</sup>. The coupled-cluster singles and doubles wave-function<sup>46</sup> is given as:

$$|\psi\rangle_{CC} = e^{\hat{T}_1 + \hat{T}_2} |\psi\rangle_{HF}, \quad e^{\hat{T}_1 + \hat{T}_2} = \mathbb{I} + \hat{T}_1 + \left(\hat{T}_2 + \frac{1}{2}\hat{T}_1^2\right) + \left(\hat{T}_2\hat{T}_1 + \frac{1}{6}\hat{T}_1^3\right) + \left(\frac{1}{2}\hat{T}_2^2 + \frac{1}{2}\hat{T}_2\hat{T}_1^2 + \frac{1}{24}\hat{T}_1^4\right) + \dots \tag{4}$$

where  $\hat{T}_1$  operator and  $\hat{T}_2$  operator are defined by their action on the HF state to generate all the possible single and double excitations respectively, and are represented in the following manner:

$$\hat{T}_{1} | \psi \rangle_{HF} = \sum_{i}^{occ} \sum_{a}^{vir} \hat{a}_{a}^{\dagger} \hat{a}_{i} t_{i}^{a} | \psi \rangle_{HF} = \sum_{i}^{occ} \sum_{a}^{vir} t_{i}^{a} | \phi_{i}^{a} \rangle, \quad \hat{T}_{2} | \psi \rangle_{HF} = \sum_{i < j}^{occ} \sum_{a < b}^{vir} t_{i}^{ab} \hat{a}_{a}^{\dagger} \hat{a}_{b}^{\dagger} \hat{a}_{i} \hat{a}_{j} | \psi \rangle_{HF} = \sum_{i < j}^{occ} \sum_{a < b}^{vir} t_{ij}^{ab} | \phi_{ij}^{ab} \rangle$$

$$(5)$$

where *vir* represents the virtual orbitals. These  $t_i^a$  and  $t_{ij}^{ab}$  parameters, obtained through CCSD-level calculation are used for initialization of a "local" approximation of the Unitary Cluster Jastrow (UCJ) ansatz<sup>47</sup>. The UCJ ansatz of L layers is given as:

$$|\psi\rangle_{UCJ} = \Pi^{L}_{\mu=1} e^{\hat{K}_{\mu}} e^{i\hat{J}_{\mu}} e^{-\hat{K}_{\mu}} |\psi\rangle_{HF}, \quad \hat{K}_{\mu} = \sum_{pq,\sigma} K^{\mu}_{pq} \hat{a}^{\dagger}_{p\sigma} \hat{a}_{q\sigma}, \quad \hat{J}_{\mu} = \sum_{pq,\sigma\tau} J^{\mu}_{pq,\sigma\tau} \hat{n}_{p\sigma} \hat{n}_{q\tau}, \tag{6}$$

where  $\hat{K}_{\mu}$ ,  $\hat{J}_{\mu}$  are the orbital rotation operators and diagonal Coulomb operators respectively and  $\hat{n}_{p\sigma}(\hat{n}_{q\tau})$  and are number operators, acting on the  $p^{th}(q^{th})$  spatial orbital and possessing  $\sigma(\tau)$  spin configuration. The orbital rotation operators can be effectively implemented using two-qubit Givens' Rotation operators<sup>48</sup>. In our case, as we are working with closed-shell systems, we employ the spin-balanced ansatz, which obeys the following conditions:

$$J^{\mu}_{pq,\alpha\alpha} = J^{\mu}_{pq,\beta\beta}, \quad J^{\mu}_{pq,\alpha\beta} = J^{\mu}_{pq,\beta\alpha} \tag{7}$$

Implementing the exact  $e^{i\hat{J}\mu}$  on a quantum computer would require the use of a fermionic SWAP network or all-to-all device connectivity. For a more localized version of the ansatz suitable to the device topology<sup>49</sup>, the appropriate sparsity constraints are added to the *J* matrices<sup>44</sup>.

### 2.3 Sample-based Quantum Diagonalization

SQD<sup>25</sup> is a combination of the quantum sampling method QSCI<sup>26</sup> and an error-mitigation technique introduced in the work, S-CoRe, which "recovers" the noisy configurations. These configurations thus obtained create a sub-space, which is further expanded, and then the projection sub-space is obtained over which SCI<sup>27</sup> is performed to obtain the ground state energy.

#### 2.3.1 Quantum State Preparation and Sampling

We begin with the goal of approximation of the ground state energy of a many-body Hamiltonian by constructing and (classically) diagonalizing a reduced Hilbert space that contains the *dominant configurations* contributing to the ground state configuration, *sampled using a quantum computer*. Starting from an approximate ground state, like  $|\psi\rangle_{HF}$ , a variational ansatz is initialized with suitable parameters:  $|\psi\rangle_{init} = \hat{U}(\theta_1, \theta_2, ..., \theta_n) |\psi\rangle_{HF}$  (in our case, the LUCJ ansatz with CCSD parameters) to increase the overlap between the trial state with the true ground state, as provided in Fig. 1.

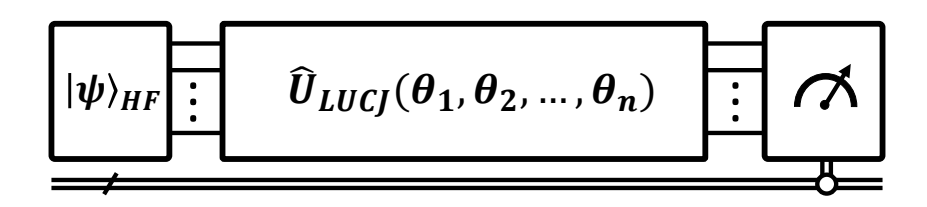


**Figure 1.** Quantum Circuit Diagram for performing Sample-based Quantum Diagonalization. The initial state is prepared as the Hartree-Fock configuration, and is acted upon by an LUCJ ansatz which is pre-initialized with  $t_i^a$  and  $t_{ij}^{ab}$  parameters obtained through CCSD calculation. Finally, measurement is performed in the  $\hat{\sigma}_z$  basis.

Quantum sampling is performed in the computational basis, and a set  $\mathcal{S}_{samp}$  is obtained with d configurations:

$$\mathscr{S}_{samp} = \{ |\phi_1\rangle, |\phi_2\rangle, ..., |\phi_d\rangle \} \tag{8}$$

where every  $|\phi_i\rangle$  can be represented as a tensor product of the  $\alpha$  spin and  $\beta$  spin configurations:  $|\phi_i\rangle = |\alpha_i\rangle \otimes |\beta_i\rangle$ . The total number of electrons in the molecular systems is designated as  $N_{elec}$ , and correspondingly the number of electrons in  $\alpha$  configuration and  $\beta$  configurations are designated as  $N_{\alpha}$  and  $N_{\beta}$  respectively. For molecular systems which contain fully-filled spatial orbitals (closed-shell) and which possess zero spin, the following conditions must be satisfied for all the computational basis states contributing to the eigen-states of the system:

$$N_{\alpha} + N_{\beta} = N_{elec}; \quad N_{\alpha} - N_{\beta} = 0. \tag{9}$$

Due to the noisy nature of quantum computers, we end up also sampling configurations which violate the particle-number and spin-z symmetries mentioned in Eq.(9). These "noisy" configurations are recovered using configuration recovery<sup>25</sup>.

#### 2.3.2 Self-Consistent Iterative Configuration Recovery

S-CoRe, or Configuration Recovery, is an iterative procedure designed to restore the sampled noisy configurations. Given an approximate ground-state occupation number distribution for the state-vector  $|\Psi\rangle$ :

$$n_{p\sigma} = \langle \Psi | \hat{a}_{p\sigma}^{\dagger} \hat{a}_{p\sigma} | \Psi \rangle, \tag{10}$$

where  $n_{p\sigma}$  is the occupancy corresponding to the  $p^{th}$  spatial orbital with  $\sigma$  spin configuration, S-CoRe updates each sampled configuration, over multiple batches (number of batches is denoted by K) by probabilistically flipping occupations of the spin-orbitals based on the values of  $n_{p\sigma}$  until the total electron number and spin projection match the target values. This produces a set of corrected configuration sub-spaces  $\mathscr{S}_{CR}^{(b)}, \forall b \in K$  that respect the intended symmetries while remaining close to the original sampled distribution.

For projection and diagonalization, the sub-spaces  $\mathscr{S}_{CR}^{(b)}$  are converted to  $\mathscr{S}_{proj}^{(b)}$  as detailed in Sec. 2.3.3. With the  $E^{(b)}$  and  $|\Psi^{(b)}\rangle$  obtained post the classical diagonalization for all the K batches, the lowest energy  $min_bE^{(b)}$  is taken as the current best estimate, and the average orbital occupation is thus calculated as:

$$n_{p\sigma} = \frac{1}{K} \sum_{b=1}^{K} \langle \boldsymbol{\psi}^{(b)} | \hat{a}_{p\sigma}^{\dagger} \hat{a}_{p\sigma} | \boldsymbol{\psi}^{(b)} \rangle, \tag{11}$$

which is again used in the next iteration and so on. This self-consistent iteration ensures that the symmetry constraints are enforced, and the recovered sub-space contains configurations closer to the desired orbital occupation distribution. From these recovered configurations at each iteration, K batches of subspaces  $\{\mathscr{S}_{CR}^{(b)}\}_{b\in K}$  are obtained.

#### 2.3.3 Selected Configuration Interaction

For the set of configurations obtained in the  $b^{th}$  batch, the sub-space is designated as  $\mathscr{S}_{CR}^{(b)}$ . As the subsequent steps remain the same for all the batches, we shall drop the super-script and denote the sub-space as  $\mathscr{S}_{CR}$  without loss of generality.

In SQD, the configurations  $\mathscr{S}_{CR} = \{ |\alpha_1\rangle \otimes |\beta_1\rangle, |\alpha_2\rangle \otimes |\beta_2\rangle, ..., |\alpha_d\rangle \otimes |\beta_d\rangle \}$  do not represent the sub-space onto which the Hamiltonian is projected. Instead in the case of **closed-shell systems** all the unique alpha configurations  $\mathscr{A}_{unique} = \{ |\alpha_1\rangle, |\alpha_2\rangle, ..., |\alpha_d\rangle \}$  and unique beta configurations  $\mathscr{B}_{unique} = \{ |\beta_1\rangle, |\beta_2\rangle, ..., |\beta_d\rangle \}$  are again made into a final set:

$$\mathcal{P}_{unique} = \mathcal{A}_{unique} \cup \mathcal{B}_{unique}$$
 (12)

Now, a new configuration space is obtained from the tensor product of  $\mathcal{P}_{unique}$  with itself, which we define as  $\mathcal{S}_{proj}$ :

$$\mathscr{P}_{unique} \otimes \mathscr{P}_{unique} = \mathscr{S}_{proj} = \{ |\lambda\rangle \otimes |\phi\rangle : \forall |\lambda\rangle \in \mathscr{P}_{unique}, \forall |\phi\rangle \in \mathscr{P}_{unique} \}. \tag{13}$$

Hence,  $\mathscr{S}_{proj}$  is the **sub-space onto which the Hamiltonian is projected onto, and not the**  $\mathscr{S}_{CR}$  obtained after configuration recovery.  $\mathscr{S}_{proj}$  is subsequently diagonalized using Davidson's Algorithm<sup>50</sup>. The construction in which the unique configurations from  $\mathscr{A}_{unique}$  and  $\mathscr{B}_{unique}$  are merged into  $\mathscr{P}_{unique}$ , followed by forming the tensor-product space  $\mathscr{P}_{unique} \otimes \mathscr{P}_{unique}$ , is motivated by the observation that the ground-state wavefunction usually exhibits correlated contributions from configuration pairs. In particular, if a configuration of the form  $|\alpha\rangle \otimes |\beta\rangle$  carries a non-zero amplitude in the ground state, then it is typically the case that the corresponding configuration  $|\beta\rangle \otimes |\alpha\rangle$  also contributes with comparable weight<sup>35</sup>.

The Hamiltonian is projected (for every  $b^{th}$  sub-space) into the sub-space  $\mathcal{S}_{proj}$ ,

$$\hat{H}_{\mathscr{S}_{proj}} = \hat{P}_{\mathscr{S}_{proj}} \hat{H} \hat{P}_{\mathscr{S}_{proj}}, \qquad \hat{P}_{\mathscr{S}_{proj}} = \sum_{\mathbf{x} \in \mathscr{S}_{proj}} |\mathbf{x}\rangle \langle \mathbf{x}|, \tag{14}$$

and the solution is obtained by performing diagonalization using Davidson's method<sup>50</sup>, finally providing us  $E^{(b)}$  and  $|\Psi^{(b)}\rangle$ , which are again utilized in Eq. (11) to obtain the average orbital occupancies.

Because the diagonalization cost scales polynomially in  $|\mathscr{S}_{proj}|$ , the method remains tractable as long as the number of selected configurations does not grow exponentially with system size<sup>50</sup>.

### 2.4 Density Matrix Embedding Theory

DMET<sup>51</sup> may be interpreted as a frequency-independent high-level embedding approach similar to Dynamical Mean-Field Theory (DMFT)<sup>52</sup>, in which the local Green's functions are substituted with the reduced density matrices of the impurity within a self-consistent procedure.

The idea behind DMET can be interpreted as the creation of a set of entangled orbitals for a given set of user-defined "fragment orbitals" in the Atomic Orbital (AO) basis, such that the correlation of the whole environment with the fragment is sufficiently captured by these entangled orbitals, also called "bath orbitals".

We denote the fragment orbital set by  $A_y$  and the remaining orbital space (the environment) by  $Env_y$ . The latter can be partitioned as

$$Env_{y} = B_{y} \cup Cor_{y} \cup Vir_{y}, \tag{15}$$

where  $B_y$  are the bath (entangled) orbitals,  $Cor_y$  are unentangled occupied (core) orbitals, and  $Vir_y$  are unentangled virtual orbitals. The sizes of these sets are  $L_{A_y}$ ,  $L_{Env_y}$ ,  $L_{B_y}$ ,  $L_{Cor_y}$ ,  $L_{Vir_y}$  respectively.

The DMET bath construction begins from a mean-field (typically Hartree–Fock) reference state. The one-particle reduced density matrix (1-RDM) of this reference wave-fucntion is projected onto the fragment subspace  $A_y$ . Diagonalizing this projected 1-RDM yields a set of eigenvalues  $\{\varepsilon_i\}$  and eigenvectors that define the fragment–environment entanglement structure. By Cauchy's interlacing theorem<sup>53</sup>, all eigenvalues satisfy  $0 \le \varepsilon_i \le 2$ . Furthermore, at most  $L_{A_y}$  eigenvalues can lie strictly between 0 and 2, corresponding to the maximum number of entangled fragment–environment degrees of freedom, according to MacDonald's theorem<sup>54</sup>. These fractionally occupied eigenvectors define the so-called "bath orbitals"  $B_y$ , which are selected by applying an occupancy threshold  $\varepsilon_{occ}$  to distinguish the entangled environment orbitals  $(B_y)$  from the unentangled core  $(Cor_y)$  and virtual  $(Vir_y)$  orbitals. Depending on  $\varepsilon_{occ}$ , the number of bath orbitals selected can be less than the number of fragment orbitals  $(L_{B_y} \le L_{A_y})$ .

In Fig. 2, a water molecule  $(H_2O)$  is selected, and the right-side hydrogen atom is treated as a fragment. The iso-spheres of the fragment orbitals and bath orbitals are visualized.

The fragment and bath orbitals are collectively designated as "impurity orbitals". The embedding Hamiltonian  $\hat{H}_{emb}^{y}$  for the local fragment  $A_{y}$  is written as a projection over this impurity space in he following manner<sup>36</sup>:

$$\hat{H}_{emb}^{y} = \sum_{rs}^{L_{A_{y}} + L_{B_{y}}} \overline{h}_{rs}^{y} \hat{a}_{r}^{\dagger} \hat{a}_{s} + \sum_{pars}^{L_{A_{y}} + L_{B_{y}}} (pq|rs) \hat{a}_{p}^{\dagger} \hat{a}_{r}^{\dagger} \hat{a}_{s} \hat{a}_{q}; \quad \overline{h}_{rs}^{y} = t_{rs} + \sum_{mn}^{L_{Cory}} [(rs|mn) - (rn|ms) D_{mn}^{Cory}]$$
(16)

where  $D_{mn}^{Cor_y}$  is the 1-RDM of the orbitals belonging to  $Cor_y$ , whereas  $\hat{a}^{\dagger}$  and  $\hat{a}$  represent the creation and annihilation operators in the molecular orbital basis. Using this method allows us to represent the correlations through the  $B_y$  and  $Cor_y$ . The

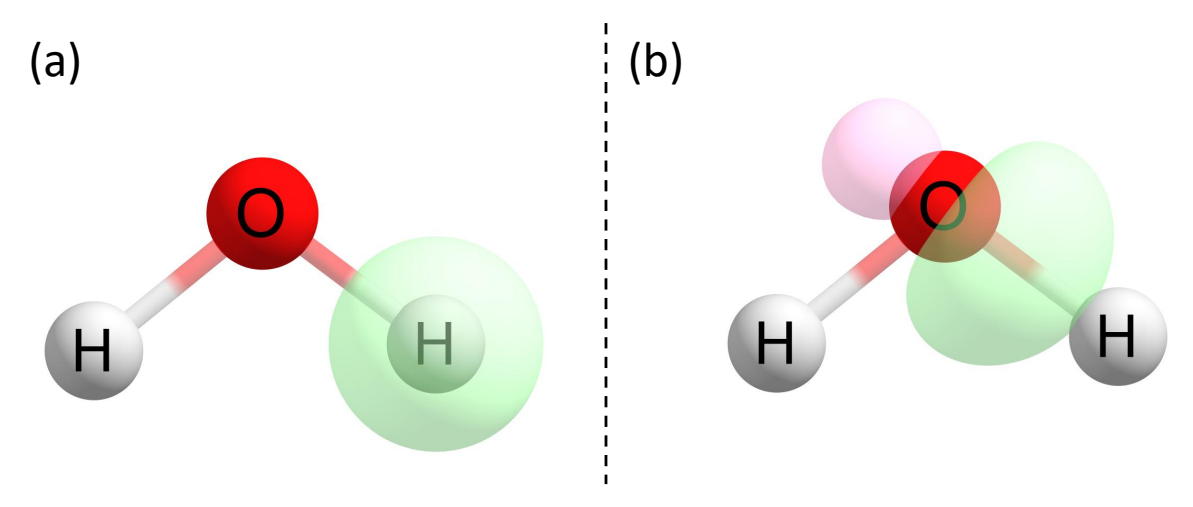


**Figure 2.** Illustrative example of bath-orbital construction for the  $H_2O$  molecule in the STO-3G basis. The system is fragmented so that the orbital localized on a single hydrogen atom constitutes the fragment. (a) shows an iso-surface of this fragment orbital; (b) shows the corresponding bath orbital obtained via DMET, which is a linear combination of the remaining localized spatial orbitals in the molecular orbital basis. Together, (a) and (b) span the impurity subspace for the H-fragment.

one-particle co-efficient terms of  $\hat{H}_{emb}^{y}$ , denoted as  $\overline{h}_{rs}^{y}$ , account for the mean-field energy of the core orbitals ( $Cor_{y}$ ). Written explicitly, the 1-RDM and 2-RDM of the fragment  $A_{y}$  can be given as  $^{36}$ :

$$D_{sr}^{y} = \langle \hat{a}_{r}^{\dagger} \hat{a}_{s} \rangle, \quad P_{ap|sr}^{y} = \langle \hat{a}_{p}^{\dagger} \hat{a}_{r}^{\dagger} \hat{a}_{s} \hat{a}_{q} \rangle; \quad pqrs \in A_{y}$$

$$(17)$$

The RDMs allow us to calculate the energies and the number of electrons for each "impurity", or "embedded Hamiltonian". A global chemical potential  $\mu_{glob}$  is introduced to ensure that the sum of the electrons in these local "impurity" fragments is equal to  $N_{occ}$  or, the total number of electrons in the whole system. This value is thus iteratively corrected until convergence in the following manner:

$$\hat{H}_{emb}^{y} \longleftarrow \hat{H}_{emb}^{y} - \mu_{glob} \sum_{r \in A_{y}} \hat{a}_{r}^{\dagger} \hat{a}_{r} \tag{18}$$

This  $\mu_{glob}$  is the same for all the orbital(r) and fragment(y) indices, hence the name "global chemical potential". This approach, where the correlations between  $A_y$  and  $B_y$  are captured, is called the "interacting bath formulation", and this mirrors the "non-interacting bath formulation", where only the correlations within the fragment orbitals are calculated, and a separate correlation potential is used. As only  $\mu_{glob}$  is optimized here, without any correlation potential optimization, this approach is also known as "one-shot embedding" The fragment energy  $(E_{A_y})^{36}$  obtained from the embedded Hamiltonians  $\hat{H}_{emb}^y$  is represented in the following manner using Eqn. 16:

$$E_{A_{y}} \approx \sum_{p \in A_{y}} \left( \sum_{q}^{L_{A_{y}} + L_{B_{y}}} \left( \frac{t_{pq} + \overline{h}_{pq}^{y}}{2} \right) D_{qp}^{y} + \frac{1}{2} \sum_{qrs}^{L_{A_{y}} + L_{B_{y}}} (pq|rs) P_{qp|sr}^{y} \right). \tag{19}$$

## 3 Methodology

This section describes the DMET-SQD framework, integrating fragmentation, impurity solving, and self-consistent quantum procedures via global chemical potential. Sec. 3.1 details the workflow; Sec. 3.2 covers hardware, software, and settings.

## 3.1 DMET-SQD Workflow

The workflow<sup>13</sup> used to perform DMET-SQD is as follows:

- 1. The molecular co-efficient matrix *C*, and the HF determinant (in the case of single-reference systems) of the whole system are obtained using Restricted HF method (here we only encounter molecular systems with fully filled spatial orbitals).
- 2. Then, the molecular spatial orbitals are localized (using Meta-Löwdin localization<sup>55</sup>) and based on the user-defined criteria (in this case, one atom per fragment), the orbitals are fragmented.

- 3. The bath orbitals are constructed with the remaining environment orbitals for the fragment  $A_y$ . Here, the occupation threshold  $\varepsilon_{occ}$  is set to  $10^{-13}$  for discarding virtual orbitals  $^{36}$ .
- 4. The Fock matrix  $\hat{F}_{imp}$  (where  $imp = A_y + B_y$ ) for each of the impurities is obtained, and the chemical potential  $\mu_{glob}$  is subtracted from the diagonal entries corresponding to the fragment orbitals:

$$\hat{F}_{imp}^{new}(\mu_{glob}) = \hat{F}_{imp} - \mu_{glob}\hat{P}_{frag}, \quad \hat{P}_{frag} = \begin{cases} 1 & \text{if } i = j \text{ and } i \in A_y \\ 0 & \text{otherwise} \end{cases}$$
(20)

- 5. Using  $\hat{F}_{imp}^{\text{new}}(\mu_{\text{glob}})$  from Eq. (20), an SCF calculation is carried out in the impurity space to obtain updated molecular properties, such as the impurity coefficient matrix  $C_{imp}^{\text{new}}(\mu_{\text{glob}})$  and the corresponding one-particle density matrix  $D^y(\mu_{\text{glob}})$ . The standard convention is to initialize  $\mu_{glob}^{init}=0$ .
- 6. Now, we use SQD, as the high-level solver to estimate the ground state energy and eigen-vector of these "impurities". The one-electron  $(h_{imp}^{pq}(\mu_{glob}))$  and two-electron  $(h_{imp}^{pqrs}(\mu_{glob}))$  Hamiltonian terms (where  $pqrs \in imp$ ) obtained after the localization, serve as the  $\hat{H}_{emb}(\mu_{glob})$ , and the configurations obtained through quantum sampling (and subsequent Configuration Recovery) are used to form the subspace onto which  $\hat{H}_{emb}$  is projected. In the case of calculating the reference energies, this step would be replaced by FCI, without any loss of generalization.
- 7. Using the eigen-vector obtained in the previous step, the following quantities are calculated:
  - fragment energy  $E_{A_v}(\mu_{glob})$  using Eq. (19),
  - number of electrons in the fragment <sup>13</sup>  $N_{A_y}^{ele}$ , where  $N_{A_y}^{ele}(\mu_{glob}) = \sum_{p \in A_y} D_{pp}^y(\mu_{glob})$
  - 1-RDM  $D^{y}_{pq}(\mu_{glob})$  and
  - 2-RDM  $P_{qp|sr}^{y}(\mu_{glob})$  of the impurities, where  $pqrs \in imp$ .
- 8. Now similar to the fragment  $A_y$ , the steps 2 to 6 are repeated for all the remaining  $N_{frag} 1$  fragments, where  $N_{frag}$  represents the number of fragments in the system. The total energy  $E_{tot}(\mu_{glob})$ , the number of electrons of the system  $N_{tot}$ , and the error in electron number  $N_{ele}^{err}$  can be thus obtained by:

$$E_{tot}(\mu_{glob}) = E_{nuc} + \sum_{v}^{N_{frag}} E_{A_{v}}(\mu_{glob}), \quad N_{tot}(\mu_{glob}) = \sum_{v}^{N_{frag}} N_{A_{v}}^{ele}(\mu_{glob}), \quad N_{err}^{ele}(\mu_{glob}) = N_{tot}(\mu_{glob}) - N_{true}$$
 (21)

where  $E_{nuc}$  is the nuclear repulsion energy of the total system, and  $N_{true}$  is the exact number of electrons in the system (which we know a priori).

9. Next, the root of the function  $N_{err}^{ele}(\mu_{glob})$  is computed to within the convergence threshold  $\varepsilon_{conv}$ , by iteratively updating  $\mu_{glob}$ , and repeating the steps 2 to 7, using a root finding method (in this case we use Newton-Secant method<sup>56</sup>). In other words, we wish to obtain a  $\mu_{glob}^{\star}$  such that:

$$\left|N_{tot}(\mu_{elob}^{\star}) - N_{true}\right| < \varepsilon_{conv}. \tag{22}$$

The above given workflow can be segmented out into six major sections, in the following manner: **Step 1**, **Step 2** can be considered to fall under a common section, designated as **Part I**, which deals with initial low-level solving of the entire system to obtain certain pre-requisites, **Steps 3**, **4** and **5**, deal with the creation of bath orbitals, and the inclusion of  $\mu_{glob}$  into the hamiltonians of the impurities, which can be designated as **Part II**. **Step 6** falls under **Part III**, where the previously obtained Hamiltonians are solved using a high-level solver, such as SQD. **Step 7** involves obtaining the relevant information from the state-vector obtained from high-level solving. This crucial step allows us to perform further iterations, and can be designated as **Part IV**. **Step 8** and **Step 9** involve looping over the fragments to obtain the total energy and the number of electrons in the system, and subsequently tweaking  $\mu_{glob}$  to satisfy Eq. (22), respectively. These steps are designated as **Part V** and **Part VI**. A diagrammatic workflow with the above-mentioned parts is provided in Fig. 3.

#### 3.2 Experimental Details

The sampling part of the quantum simulation experiments in this work was executed on the Eagle R3 quantum processor (IBM Sherbrooke, containing 127 qubits)<sup>49</sup>. The corresponding hardware calibration metrics recorded immediately prior to the computation are provided in Table 1. These values represent the initial calibration state of the device and should not be interpreted as a faithful reflection of the noise characteristics during execution. This distinction is important, as the full set of molecular simulations required approximately two days to complete, largely due to queueing delays between successive quantum-sampling jobs, *during which hardware performance may drift*.

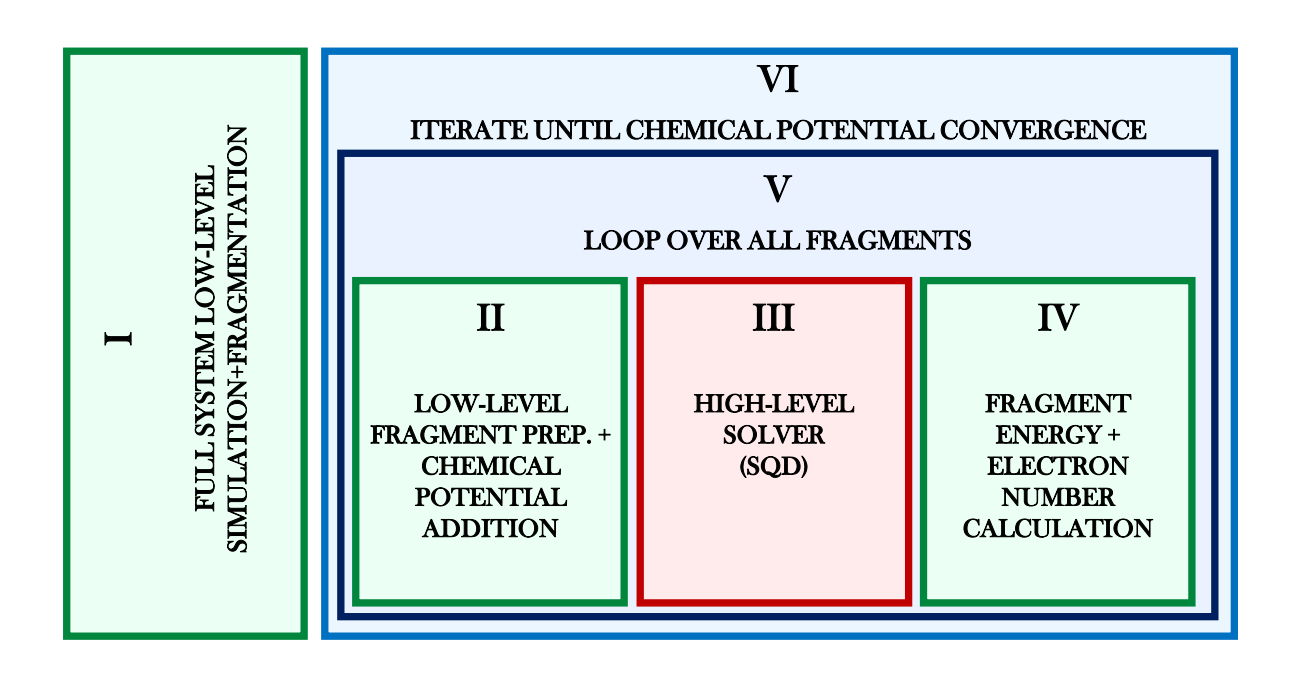


**Figure 3.** A simplified workflow for DMET-SQD

For DMET-SQD and DMET-FCI, Tangelo v0.4.3<sup>57</sup> was used. LUCJ circuits were generated using ffsim v0.10.0<sup>58</sup>, and quantum circuits were constructed and transpiled with Qiskit v1.4.2<sup>59</sup> and Qiskit IBM Runtime v0.36.1. All quantum-chemistry tasks (HF, CCSD, and SCI) were carried out using PySCF v2.10.0<sup>55</sup>. The root-finding method used was the Newton–Secant method from scipy v1.15.3<sup>60</sup>.

The molecules taken for the study are shown in Table 3. The STO-3G basis set was employed in this work, due to its minimal size and computational efficiency, which make it particularly well suited for quantum simulations on current NISQ-era hardware, and the fragmentation was performed such that each atom in the fragment is treated as a fragment for all the molecules. The number of shots used for quantum sampling was  $10^4$  and was kept consistent across all the impurities, regardless of the number of spin orbitals within them. For each impurity, 5 iterations of S-CoRe were performed. The maximum allowed samples per batch was set to  $10^5$ . The circuits were transpiled<sup>62</sup> with optimization set to level 3, and no additional error handling techniques were employed in these series of experiments. The convergence threshold  $\varepsilon_{conv}$  for  $\mu_{glob}$  was set to  $1.48 \times 10^{-8}$ , which is the default parameter in scipy.optimize.newton method.

#### 4 Results and Discussion

The absolute energy differences between the DMET-SQD energies and DMET-FCI energies of the molecules are presented in Fig. 4. As is evident, the energy differences obtained are consistently lower than  $10^{-5}$  Ha, and in some cases are within micro-Hartree precision in comparison to DMET-FCI.

The details pertaining to the fragmentation settings, quantum resource requirements, and the dimensions of the symmetry space and Hilbert space are summarized in Table 2. The resource estimation is presented in the IBM Sherbrooke superconducting hardware basis gate set  $\{X, R_z, \sqrt{X}(S_x), ECR\}$ . The largest quantum-sampling experiment employed 30 qubits, with a symmetry-space dimension of 25,050,025 and a Hilbert-space dimension of 1,073,741,824. The largest quantum circuit depth was 1081. These entries have been highlighted in the table to indicate the maximal values observed in our study.

The simulation results showing the energies obtained through DMET-SQD on a quantum computer, DMET-FCI as reference, and the absolute energy difference between them are shown in Table 3. The energy differences lie along the range of micro-Hartree, indicating strong agreement with the reference. The geometric co-ordinates of the molecules used for simulation were geometry-optimized (force-field level)<sup>63</sup> and are given in the supplementary section (S1).

These results indicate that the quantum sampling, configuration recovery and subsequent creation of projection sub-space through symmetrized expansion of the unique spin configurations (Eq. 12 and Eq. 13), is leading to diagonalization over a sub-space which is a sizable fraction of the *symmetry space*<sup>35</sup>.

**Table 1.** Calibration metrics for the Eagle R3 processor (IBM Sherbrooke, containing 127 qubits) recorded on 4 June 2025 at 01:48:22 EST. These values correspond to the device's pre-execution calibration snapshot, including coherence times ( $T_1$ ,  $T_2$ ), qubit frequency, anharmonicity, readout assignment errors, gate error rates, and gate durations<sup>61</sup>.

Parameter	Value
T1	270.447138 μs
T2	211.026521 μs
Frequency	4.794027 GHz
Anharmonicity	-0.310939 GHz
Readout assignment error	0.021240
P(0   1)	0.020507
P(1   0)	0.019042
Readout length	1216.0 ns
Identity gate error	0.000244
$R_z$ gate error	0.0
$\sqrt{X}$ ( $S_x$ ) gate error	0.000244
Pauli-X gate error	0.000244
ECR gate error	0.006767
Gate time	533.333333 ns

Moreover, SQD's reliance on recovering signal from noisy configurations, evidenced by the need for only 2% meaningful signal amid raw noisy data in benchmark cases<sup>25</sup>, reveals a deep hardware dependence that, while enabling NISQ-scale simulations, introduces inefficiencies tied to noise levels. In lower-noise regimes (higher signal configurations), the subspace dimension d could remain fixed, but fewer invalid configurations would require correction via the iterative orbital occupancy updates, potentially shifting the burden to the quantum sampler itself. Sampling from this single ansatz distribution, however, introduces key caveats<sup>28</sup>: notably, the risk of repetitive over-sampling of dominant configurations, leaving scant opportunity to capture rarer determinants that contribute non-negligibly to the true ground state.

Although lower hardware noise increases the fidelity of sampled configurations, it simultaneously suppresses the population of symmetry-breaking configurations. Configuration Recovery relies upon these noisy configurations to expand the sampled subspace using the orbital-occupancy distribution as a reference. In the extreme low-noise limit, this reduced exploration can narrow the recoverable determinant space and ultimately degrade the accuracy of SQD. Modern trapped-ion platforms routinely achieve single- and two-qubit gate fidelities of 99.99% and 99.9% $^{64}$ , neutral-atom arrays report two-qubit fidelities approaching 99.5% $^{65}$ , and superconducting qubits have recently achieved  $\sim$  99.93% two-qubit fidelities $^{66}$ , all of which influence the balance between valid and recoverable configurations in SQD. In ultra–low-noise regimes, the sampling distribution would collapse onto a few high-weight determinants, limiting subspace diversity, whereas moderate noise will increase the off-symmetry samples needed for SQD to reconstruct correlation-relevant determinants.

## 5 Conclusion

In this study, we have successfully performed quantum simulation of a set of natural ligand-like molecules in the STO-3G basis set (whose molecular weights are between 40 Da and 76 Da). We employed DMET as a classical fragmentation technique followed by SQD as a high-level solver. The simulations were run on IBM's Eagle R3 (IBM Sherbrooke) superconducting quantum computing hardware. All the results obtained were benchmarked against DMET-FCI and were found to be within chemical accuracy.

Thereby, the current NISQ hardware seems to show potential to perform quantum sampling experiments, leading to classical sub-space diagonalization in post-processing with high accuracy. This paves the way for potential industrial use-cases in the field of quantum computer-aided drug design and materials design.

That being said, although SQD ensures that the noisy configurations are recovered into the symmetry space by using the average orbital occupancy distributions as reference, this does not guarantee that the noisy configurations are stochastically converted into determinants with a non-negligible contribution to the true ground state. The procedure still might lead to obtaining configurations from the symmetry space, which contribute little to the final energy estimate.

This highlights the need for approaches that explicitly promote compactness in the selected subspace, where the retained configurations are guided by user-defined criteria rather than by sampling alone. By constraining the search to a compact and size-controlled subspace, one can more reliably concentrate quantum and classical resources only on the determinants most relevant to the target state, leading to an overall reduction of computational cost for the procedure.

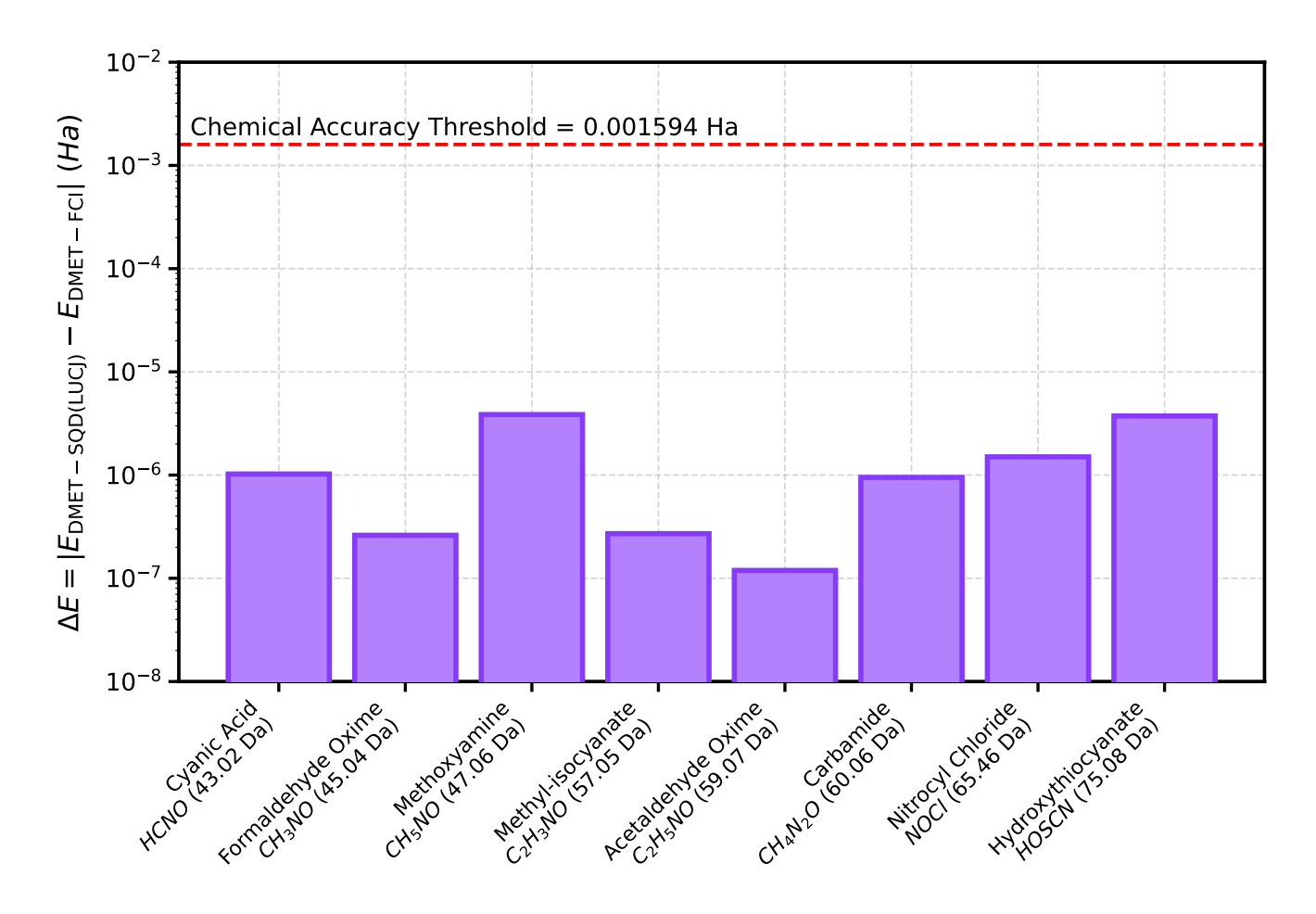


**Figure 4.** Comparison of the DMET-SQD energies obtained for the set of studied molecules on IBM Sherbrooke Quantum Hardware ( $4^{th} - 5^{th}$  June, 2025) with DMET-FCI. All the energies obtained are within the chemical accuracy criterion (1 kcal/mol  $\approx 0.001594$  Ha), which is marked with the red-dashed line. The x-axis denotes the name of the studied molecule, the molecular formula and the molecular weight. The y-axis denotes the absolute energy difference between the energy obtained through quantum hardware using DMET-SQD ( $E_{DMET-SQD}$ ) and the reference energy  $E_{DMET-FCI}$ , which is defined as  $\triangle E$ .

**Table 2.** Quantum resource estimation summary for the molecular fragments. Beginning from the left: Chemical formula of the molecule, Fragment, number of spatial orbitals and number of electrons represented as (o, e), number of qubits used, depth of the quantum circuit, number of  $R_z$ ,  $\sqrt{X}(S_x)$ , X, ECR gates used respectively for the specific instance of execution, dimension of the Symmetry Space(IS.SI), dimension of the Hilbert Space(IH.SI), the QPU time taken for performing DMET-SQD, and the number of iterations for  $\mu_{glob}$  convergence ( $N_{it}$ ).

Molecule	Frag	(o, e)	Qubits	Depth	$R_z$	$S_{x}$	X	ECR	IS.SI	lH.Sl	T(s)	N <sub>it</sub>
	[H]	(10, 10)	20	365	1833	1548	88	550	63,504	1,048,576		
HOGN	[O]	(10, 10)	20	343	1804	1410	126	550	63,504	1,048,576	60	4
HOCN	[C]	(10, 10)	20	389	1939	1524	108	584	63,504	1,048,576	68	4
	[N]	(2, 2)	4	34	46	38	0	12	4	16		
	[C]	(10, 10)	20	366	1847	1454	134	580	63,504	1,048,576		
	[H]	(2, 2)	4	34	43	38	0	12	4	16		
CH <sub>3</sub> NO	[H]	(2, 2)	4	34	44	38	0	12	4	16	107	4
	[H]	(2, 2)	4	35	47	38	0	12	4	16		4
	[N]	(10, 10)	20	341	1814	1511	88	542	63,504	1,048,576		
	[O]	(10, 10)	20	378	1893	1479	138	586	63,504	1,048,576		
	[C]	(10, 10)	20	369	1946	1578	109	586	63,504	1,048,576		
	[H]	(2, 2)	4	35	45	38	0	12	4	16		
	[H]	(2, 2)	4	35	48	38	0	12	4	16		
CHNO	[H]	(2, 2)	4	34	44	38	0	12	4	16	4.5.5	4
CH <sub>5</sub> NO	[H]	(2, 2)	4	35	46	38	0	12	4	16	130	
	[H]	(2, 2)	4	34	46	38	0	12	4	16		
	[O]	(10, 10)	20	369	1796	1463	120	552	63,504	1,048,576		
	[N]	(10, 10)	20	410	1950	1543	130	590	63,504	1,048,576		
	[C]	(10, 10)	20	591	1929	1597	126	604	63,504	1,048,576		
	[C]	(10, 10)	20	396	1871	1503	125	578	63,504	1,048,576		4
	[H]	(2, 2)	4	35	46	38	0	12	4	16		
$C_2H_3NO$	[H]	(2, 2)	4	35	46	38	0	12	4	16	130	
	[H]	(2, 2)	4	34	43	38	0	12	4	16		
	[N]	(10, 10)	20	371	1901	1532	104	568	63,504	1,048,576		
	[O]	(10, 10)	20	383	1868	1544	116	572	63,504	1,048,576		
	[C]	(10, 10)	20	361	1927	1589	107	580	63,504	1,048,576		
	[C]	(10, 10)	20	343	1813	1432	134	568	63,504	1,048,576		
	[H]	(2, 2)	4	35	47	38	0	12	4	16		
	[H]	(2, 2)	4	35	47	38	0	12	4	16		
$C_2H_5NO$	[H]	(2, 2)	4	35	46	38	0	12	4	16	165	4
	[H]	(2, 2)	4	35	48	38	0	12	4	16		
	[H]	(2, 2)	4	35	48	38	0	12	4	16		
	[N]	(10, 10)	20	375	1906	1545	94	568	63,504	1,048,576		
	[O]	(10, 10)	20	635	1865	1424	139	572	63,504	1,048,576		
	[C]	(10, 10)	20	633	1809	1405	142	568	63,504	1,048,576		
	[N]	(10, 10)	20	655	1877	1389	131	588	63,504	1,048,576		
CH <sub>4</sub> N <sub>2</sub> O	[H]	(2, 2)	4	34	43	38	0	12	4	16		
	[H]	(2, 2)	4	35	47	38	0	12	4	16	110	
	[H]	(2, 2)	4	34	44	38	0	12	4	16	119	4
	[H]	(2, 2)	4	33	42	38	0	12	4	16		
	[N]	(10, 10)	20	408	1925	1500	117	578	63,504	1,048,576		
	[O]	(10, 10)	20	444	1811	1437	122	564	63,504	1,048,576		
NOCl	[N]	(8, 10)	16	223	897	628	88	300	3,136	65,536		
	[O]	(8, 10)	16	219	891	636	80	300	3,136	65,536	62	4
	[Cl]	(12, 18)	24	342	2441	2117	109	738	48,400	16,777,216		
	[H]	(2, 2)	4	34	43	38	0	12	4	16		
	[O]	(10, 10)	20	454	1838	1427	199	619	63,504	1,048,576		
HOSCN	[S]	(15, 18)	30	1,081	4384	4018	205	1351	25,050,025	1,073,741,824	98	4
nosen	[C]	(10, 10)	20	651	1911	1534	146	600	63,504	1,048,576		
	[N]	(10, 10)	20	558	2021	1622	143	646	63,504	1,048,576		

**Table 3.** Energy results obtained from the DMET–SQD simulations for the studied molecules.  $\Delta E$  denotes the absolute energy difference between  $E_{\text{DMET-FCI}}$  and  $E_{\text{DMET-SOD}}$ , i.e.,  $\Delta E = |E_{\text{DMET-FCI}} - E_{\text{DMET-SOD}}|$  in Hartree.

Molecule	$E_{\text{DMET-SQD}}$ (Ha)	$E_{\text{DMET-FCI}}$ (Ha)	$\Delta E$ (Ha)	
Cyanic Acid	-165.80748733	-165.80748835	$1.024 \times 10^{-6}$	
(HOCN)	-103.80748733	-103.80748833	1.024 \ 10	
Formaldehyde Oxime	-166.89443901	-166.89443875	$2.611 \times 10^{-7}$	
$(CH_3NO)$	-100.89443901	-100.89443873	2.011 × 10	
Methoxyamine	-168.04584566	-168.04584180	$3.856 \times 10^{-6}$	
$(CH_5NO)$	-108:04384300	-108.04384180	3.830 × 10	
Methyl Isocyanate	-204.57166716	-204.57166689	$2.708 \times 10^{-7}$	
$(C_2H_3NO)$	-204.37100710	-204.37100089	2.708 × 10	
Acetaldehyde Oxime	-205.56816508	-205.56816496	$1.192 \times 10^{-7}$	
$(C_2H_5NO)$	-203.30810308	-203.30810490	1.192 × 10	
Carbamide / Urea	-221.44130237	-221.44130142	$9.494 \times 10^{-7}$	
$(CH_4N_2O)$	-221.77130237	-221.44130142	J.∓J∓ ∧ 10	
Nitrosyl Chloride	-582.38458086	-582.38458236	$1.501 \times 10^{-6}$	
(NOCl)	-302.30738000	-302.30430230	1.301 \ 10	
Hydroxythiocyanate	-559.05055857	-559.05056231	$3.739 \times 10^{-6}$	
(HOSCN)	-557.05055657	-337.03030231	3.737 \ 10	

## **Acknowledgements**

The authors would like to extend appreciation to the advisors of Qclairvoyance Quantum Labs for their support, constructive discussions, and inspiration throughout the preparation of this work.

## **Funding**

This research received no specific grant from any funding agency in the public, commercial, or not-for-profit sectors.

## **Competing interests**

R.M. and R.V. are paid consultants at Qclairvoyance Quantum Labs. The other authors declare no competing interests.

## References

- 1. Levine, I. N. Molecular Orbital Theory, chap. 16, 653–710 (Pearson Education, Boston, 2014). 7th Edition.
- **2.** Gao, H., Imamura, S., Kasagi, A. & Yoshida, E. Distributed implementation of full configuration interaction for one trillion determinants. *J. Chem. Theory Comput.* **20**, 1185–1192, DOI: 10.1021/acs.jctc.3c01190 (2024).
- **3.** Hehre, W. J., Stewart, R. F. & Pople, J. A. Self-consistent molecular-orbital methods. i. use of gaussian expansions of slater-type atomic orbitals. *The J. Chem. Phys.* **51**, 2657–2664, DOI: 10.1063/1.1672392 (1969).
- **4.** Fock, V. Näherungsmethode zur lösung des quantenmechanischen mehrkörperproblems. *Zeitschrift für Physik* **61**, 126–148, DOI: 10.1007/BF01340294 (1930).
- **5.** Kirsopp, J. J. M. *et al.* Quantum computational quantification of protein–ligand interactions. *Int. J. Quantum Chem.* **122**, e26975, DOI: https://doi.org/10.1002/qua.26975 (2022).
- **6.** Malone, F. D. *et al.* Towards the simulation of large scale protein–ligand interactions on nisq-era quantum computers. *Chem. Sci.* **13**, 3094–3108, DOI: 10.1039/D1SC05691C (2022).
- 7. Bowling, P. E., Broderick, D. R. & Herbert, J. M. Convergent protocols for computing protein–ligand interaction energies using fragment-based quantum chemistry. *J. Chem. Theory Comput.* 21, 951–966, DOI: 10.1021/acs.jctc.4c01429 (2025).
- **8.** Barton, D. H. R. & Cookson, R. C. The principles of conformational analysis. *Q. Rev. Chem. Soc.* **10**, 44–82, DOI: 10.1039/QR9561000044 (1956).
- **9.** Mancini, G., Fusè, M., Lazzari, F. & Barone, V. Fast exploration of potential energy surfaces with a joint venture of quantum chemistry, evolutionary algorithms and unsupervised learning. *Digit. Discov.* **1**, 790–805, DOI: 10.1039/D2DD00070A (2022).

- **10.** Anurag, K. S. V. *et al.* Potential energy surface scan of *n*-butane using various quantum chemistry software. *Authorea* DOI: 10.22541/au.174624847.78353339/v2 (2025).
- 11. Hao, Y., Ding, Q., Wang, X. & Yuan, X. Large-scale efficient molecule geometry optimization with hybrid quantum-classical computing (2025). 2509.07460.
- **12.** Shajan, A. *et al.* Towards quantum-centric simulations of extended molecules: sample-based quantum diagonalization enhanced with density matrix embedding theory. 2411.09861 (2024).
- **13.** Kawashima, Y. *et al.* Optimizing electronic structure simulations on a trapped-ion quantum computer using problem decomposition. *Commun. Phys.* **4**, 245, DOI: 10.1038/s42005-021-00751-9 (2021).
- **14.** O'Malley, P. J. J. *et al.* Scalable quantum simulation of molecular energies. *Phys. Rev. X* **6**, 031007, DOI: 10.1103/PhysRevX.6.031007 (2016).
- **15.** Schuch, N. & Verstraete, F. Computational complexity of interacting electrons and fundamental limitations of density functional theory. *Nat. Phys.* **5**, 732–735, DOI: 10.1038/nphys1370 (2009).
- **16.** Cao, Y. *et al.* Quantum chemistry in the age of quantum computing. *Chem. Rev.* **119**, 10856–10915, DOI: 10.1021/acs. chemrev.8b00803 (2019).
- **17.** Aspuru-Guzik, A., Dutoi, A. D., Love, P. J. & Head-Gordon, M. Simulated quantum computation of molecular energies. *Science* **309**, 1704–1707, DOI: 10.1126/science.1113479 (2005).
- **18.** Eisert, J. & Preskill, J. Mind the gaps: The fraught road to quantum advantage. *arXiv*:2510.19928 DOI: 10.48550/arXiv. 2510.19928 (2025).
- **19.** Kitaev, A. Quantum measurements and the abelian stabilizer problem. *arXiv:quant-ph/9511026* DOI: 10.48550/arXiv. quant-ph/9511026 (1995).
- **20.** Gilyén, A., Su, Y., Low, G. H. & Wiebe, N. Quantum singular value transformation and beyond: exponential improvements for quantum matrix arithmetics. In *Proceedings of the 51st Annual ACM SIGACT Symposium on Theory of Computing*, STOC '19, 193–204, DOI: 10.1145/3313276.3316366 (ACM, 2019).
- 21. Preskill, J. Quantum computing in the nisq era and beyond. *Quantum* 2, 79, DOI: 10.22331/q-2018-08-06-79 (2018).
- **22.** Peruzzo, A. *et al.* A variational eigenvalue solver on a photonic quantum processor. *Nat. Commun.* **5**, 4213, DOI: 10.1038/ncomms5213 (2014).
- **23.** Belaloui, N. E. *et al.* Ground-state energy estimation on current quantum hardware through the variational quantum eigensolver: A practical study. *J. Chem. Theory Comput.* **21**, 6777–6792, DOI: 10.1021/acs.jctc.4c01657 (2025).
- **24.** Tilly, J. *et al.* The variational quantum eigensolver: A review of methods and best practices. *Phys. Reports* **986**, 1–128, DOI: 10.1016/j.physrep.2022.08.003 (2022).
- **25.** Robledo-Moreno, J. *et al.* Chemistry beyond the scale of exact diagonalization on a quantum-centric supercomputer. *Sci. Adv.* **11**, eadu9991, DOI: 10.1126/sciadv.adu9991 (2025).
- **26.** Kanno, K. *et al.* Quantum-selected configuration interaction: classical diagonalization of hamiltonians in subspaces selected by quantum computers. 2302.11320 (2023).
- **27.** Evangelista, F. A. Adaptive multiconfigurational wave functions. *The J. Chem. Phys.* **140**, 124114, DOI: 10.1063/1.4869192 (2014).
- **28.** Reinholdt, P. *et al.* Critical limitations in quantum-selected configuration interaction methods. *J. Chem. Theory Comput.* **21**, 6811–6822, DOI: 10.1021/acs.jctc.5c00375 (2025).
- **29.** Alexeev, Y. *et al.* Quantum-centric supercomputing for materials science: A perspective on challenges and future directions. *Futur. Gener. Comput. Syst.* **160**, 666–710, DOI: 10.1016/j.future.2024.04.060 (2024).
- **30.** Barison, S., Robledo Moreno, J. & Motta, M. Quantum-centric computation of molecular excited states with extended sample-based quantum diagonalization. *Quantum Sci. Technol.* **10**, 025034, DOI: 10.1088/2058-9565/adb781 (2025).
- **31.** Yoshioka, N. *et al.* Krylov diagonalization of large many-body hamiltonians on a quantum processor. *Nat. Commun.* **16**, 5014, DOI: 10.1038/s41467-025-59716-z (2025).
- **32.** Campbell, E. Random compiler for fast hamiltonian simulation. *Phys. Rev. Lett.* **123**, 070503, DOI: 10.1103/PhysRevLett. 123.070503 (2019).
- 33. Yu, J. et al. Quantum-centric algorithm for sample-based krylov diagonalization. 2501.09702 (2025).

- **34.** Piccinelli, S. *et al.* Quantum chemistry with provable convergence via randomized sample-based quantum diagonalization. 2508.02578 (2025).
- **35.** Pellow-Jarman, A. *et al.* Hivqe: Handover iterative variational quantum eigensolver for efficient quantum chemistry calculations. 2503.06292 (2025).
- **36.** Wouters, S., Jiménez-Hoyos, C. A., Sun, Q. & Chan, G. K.-L. A practical guide to density matrix embedding theory in quantum chemistry. *J. Chem. Theory Comput.* **12**, 2706–2719, DOI: 10.1021/acs.jctc.6b00316 (2016).
- **37.** Caimi, P. F. *et al.* Phase i clinical trial of the base excision repair inhibitor methoxyamine in combination with fludarabine for patients with advanced hematologic malignancies. *Oncotarget* **8**, 79864–79875, DOI: 10.18632/oncotarget.20094 (2017).
- **38.** Eads, J. R. *et al.* Phase i clinical trial of temozolomide and methoxyamine (trc-102), an inhibitor of base excision repair, in patients with advanced solid tumors. *Investig. New Drugs* **39**, 142–151, DOI: 10.1007/s10637-020-00962-x (2021).
- **39.** Ghosh, A. K. & Brindisi, M. Urea derivatives in modern drug discovery and medicinal chemistry. *J. Medicinal Chem.* **63**, 2751–2788, DOI: 10.1021/acs.jmedchem.9b01541 (2020).
- **40.** Listro, R. *et al.* Urea-based anticancer agents: Exploring 100 years of research with an eye to the future. *Front. Chem.* **10**, DOI: 10.3389/fchem.2022.995351 (2022).
- **41.** Born, M. & Oppenheimer, R. Zur Quantentheorie der Molekeln. *Annalen der Physik* **389**, 457–484, DOI: 10.1002/andp. 19273892002 (1927).
- **42.** Szabo, A. & Ostlund, N. S. *Modern Quantum Chemistry: Introduction to Advanced Electronic Structure Theory*. Dover Books on Chemistry (Dover Publications, 1996). See Section 2.4.1, pp. 89–95.
- **43.** Jordan, P. & Wigner, E. Über das paulische äquivalenzverbot. *Zeitschrift für Physik* **47**, 631–651, DOI: 10.1007/BF01331938 (1928).
- **44.** Motta, M., Sung, K. J., Whaley, K. B., Head-Gordon, M. & Shee, J. Bridging physical intuition and hardware efficiency for correlated electronic states: the local unitary cluster jastrow ansatz for electronic structure. *Chem. Sci.* **14**, 11213–11227, DOI: 10.1039/D3SC02516K (2023).
- **45.** Bartlett, R. J. & Musiał, M. Coupled-cluster theory in quantum chemistry. *Rev. Mod. Phys.* **79**, 291–352, DOI: 10.1103/RevModPhys.79.291 (2007).
- **46.** Jensen, F. *Introduction to Computational Chemistry* (John Wiley & Sons, Inc., Hoboken, NJ, USA, 2006). Second Edition, see Section 4.9, pp. 169–174.
- **47.** Matsuzawa, Y. & Kurashige, Y. Jastrow-type decomposition in quantum chemistry for low-depth quantum circuits. *J. Chem. Theory Comput.* **16**, 944–952, DOI: 10.1021/acs.jctc.9b00963 (2020).
- **48.** Arrazola, J. M. *et al.* Universal quantum circuits for quantum chemistry. *Quantum* **6**, 742, DOI: 10.22331/q-2022-06-20-742 (2022).
- **49.** AbuGhanem, M. Ibm quantum computers: Evolution, performance, and future directions. *The J. Supercomput.* **81**, 687–715, DOI: 10.1007/s11227-025-07047-7 (2025).
- **50.** Davidson, E. R. The iterative calculation of a few of the lowest eigenvalues and corresponding eigenvectors of large real-symmetric matrices. *J. Comput. Phys.* **17**, 87–94, DOI: 10.1016/0021-9991(75)90065-0 (1975).
- **51.** Knizia, G. & Chan, G. K.-L. Density matrix embedding: A simple alternative to dynamical mean-field theory. *Phys. Rev. Lett.* **109**, 186404, DOI: 10.1103/PhysRevLett.109.186404 (2012).
- **52.** Georges, A., Kotliar, G., Krauth, W. & Rozenberg, M. J. Dynamical mean-field theory of strongly correlated fermion systems and the limit of infinite dimensions. *Rev. Mod. Phys.* **68**, 13–125, DOI: 10.1103/RevModPhys.68.13 (1996).
- 53. Horn, R. & Johnson, C. Matrix Analysis, chap. 4.3, 242–248 (Cambridge University Press, 2012), 2nd edn.
- **54.** MacDonald, J. K. L. Successive approximations by the rayleigh–ritz variation method. *Phys. Rev.* **43**, 830–833, DOI: 10.1103/PhysRev.43.830 (1933).
- **55.** Sun, Q. et al. The python-based simulations of chemistry framework (pyscf). 1701.08223 (2017).
- **56.** Papakonstantinou, J. M. & Tapia, R. A. Origin and evolution of the secant method in one dimension. *The Am. Math. Mon.* **120**, 500–518, DOI: 10.4169/amer.math.monthly.120.06.500 (2013).
- **57.** Senicourt, V. *et al.* Tangelo: An open-source python package for end-to-end chemistry workflows on quantum computers. 2206.12424 (2022).

- **58.** The ffsim developers. *ffsim: Faster simulations of fermionic quantum circuits, v0.0.56.* qiskit-community (2025). Accessed: 2025-11-11.
- **59.** Javadi-Abhari, A. et al. Quantum computing with qiskit. 2405.08810 (2024).
- **60.** Virtanen, P. *et al.* SciPy 1.0: Fundamental Algorithms for Scientific Computing in Python. *Nat. Methods* **17**, 261–272, DOI: 10.1038/s41592-019-0686-2 (2020).
- **61.** Krantz, P. *et al.* A quantum engineer's guide to superconducting qubits. *Appl. Phys. Rev.* **6**, 021318, DOI: 10.1063/1. 5089550 (2019).
- 62. Li, G., Ding, Y. & Xie, Y. Tackling the qubit mapping problem for nisq-era quantum devices. 1809.02573 (2019).
- 63. Landrum, G. et al. Rdkit: Open-source cheminformatics software, DOI: 10.5281/zenodo.17232453 (2025).
- **64.** Ballance, C. J., Harty, T. P., Linke, N. M., Sepiol, M. A. & Lucas, D. M. High-fidelity quantum logic gates using trapped-ion hyperfine qubits. *Phys. Rev. Lett.* **117**, 060504, DOI: 10.1103/PhysRevLett.117.060504 (2016).
- **65.** Evered, S. J. *et al.* High-fidelity parallel entangling gates on a neutral-atom quantum computer. *Nature* **622**, 268–272, DOI: 10.1038/s41586-023-06481-y (2023).
- **66.** Marxer, F. *et al.* Above 99.9% fidelity single-qubit gates, two-qubit gates, and readout in a single superconducting quantum device. 2508.16437 (2025).

## **Supplementary Information**

## **S1** Geometric Coordinates of the Studied Molecules

$\begin{array}{c ccccccccccccccccccccccccccccccccccc$	Molecule	Geometric Coordinates				
$\begin{array}{c} \text{Cyanic Acid} \\ (HOCN) \\ \\ \\ \\ \\ \\ \\ \\ \\ \\ \\ \\ \\ \\ \\ \\ \\ \\ \\$	Wiolectife	Atom				
$ \begin{array}{c ccccccccccccccccccccccccccccccccccc$		Н	-1.458587	-0.272810	0.065495	
$\begin{array}{c ccccccccccccccccccccccccccccccccccc$	Cyanic Acid		-0.600578	0.099568	-0.321249	
Formaldehyde Oxime $(C_{13}NO)$ $H$ $2.170747$ $-0.116917$ $0.612439$ $-0.507441$ $-0.00526$ $1.043453$ $-0.507441$ $-0.16917$ $0.612439$ $-0.667161$ $-0.500891$ $-0.207852$ $-0.523560$ $0.074740$ $-0.1298394$ $0.285100$ $0.293422$ $-0.668149$ $0.201296$ $0.149956$ $-0.658496$ $-0.658496$ $-0.658496$ $-0.658496$ $-0.658496$ $-0.658496$ $-0.658496$ $-0.658496$ $-0.658496$ $-0.658496$ $-0.64132$ $-0.237043$ $-0.$	(HOCN)	C	0.544407	0.090463	0.422709	
$ \begin{array}{c ccccccccccccccccccccccccccccccccccc$		N	1.514757	0.082779	1.053115	
$ \begin{array}{c ccccccccccccccccccccccccccccccccccc$		С	-0.910484	-0.020915	-0.332484	
$ \begin{array}{c ccccccccccccccccccccccccccccccccccc$		Н	2.170747	-0.116917	0.612439	
$\begin{array}{c ccccccccccccccccccccccccccccccccccc$	Formaldehyde Oxime	Н	-1.005526	1.043453	-0.507441	
$\begin{array}{c ccccccccccccccccccccccccccccccccccc$	$(CH_3NO)$	Н	-1.760983	-0.667161	-0.500891	
$\begin{array}{c ccccccccccccccccccccccccccccccccccc$		N	0.207852	-0.523560	0.074740	
$\begin{array}{c ccccccccccccccccccccccccccccccccccc$		О	1.298394	0.285100	0.293422	
$\begin{array}{c ccccccccccccccccccccccccccccccccccc$		С	-0.966149	0.201296	0.149956	
$ \begin{array}{c ccccccccccccccccccccccccccccccccccc$		Н	-1.000265	0.965450	-0.658496	
$\begin{array}{c ccccccccccccccccccccccccccccccccccc$		Н	-1.667205	0.516700	0.949826	
$(CH_5NO) \\ H \\ 1.882536 \\ 0.441132 \\ -0.409602 \\ H \\ 1.601346 \\ -1.163838 \\ -0.023188 \\ -0.023188 \\ 0.105691 \\ 0.692069 \\ -0.872655 \\ -0.048579 \\ -0.012732 \\ -0.12172 \\ 0.839315 \\ -0.612203 \\ -0.731912 \\ 0.839315 \\ -1.419752 \\ -0.612203 \\ -0.796487 \\ -1.514077 \\ 0.782782 \\ 0.345983 \\ 0.20579 \\ -0.121172 \\ 0.839315 \\ -0.612203 \\ -0.796487 \\ 0.3251223 \\ 0.500017 \\ -0.581535 \\ 0 \\ 2.615024 \\ -0.090684 \\ 0.326629 \\ -1.321954 \\ 0.079847 \\ -0.059915 \\ -0.023694 \\ -0.492848 \\ 0.731931 \\ -1.440397 \\ -0.441345 \\ -1.033016 \\ -1.440397 \\ -0.441345 \\ -1.033016 \\ -1.440397 \\ -0.441345 \\ -1.033016 \\ -1.440397 \\ -0.441345 \\ -1.033016 \\ -1.440397 \\ -0.441345 \\ -1.033016 \\ -1.488828 \\ -0.873562 \\ 0.413794 \\ -0.2186822 \\ -0.810420 \\ 0.726078 \\ -0.726078 \\ -0.726078 \\ -0.023609 \\ -0.174787 \\ 0.475047 \\ -0.475047 \\ -0.475047 \\ -0.475047 \\ -0.2122930 \\ -0.259006 \\ -0.346006 \\ -0.346006$	Methoxyamine	Н	-1.306933	-0.785003	-0.237043	
$\begin{array}{c ccccccccccccccccccccccccccccccccccc$	•	Н	1.882536	0.441132	-0.409602	
$\begin{array}{c ccccccccccccccccccccccccccccccccccc$	,	Н	1.601346	-1.163838	-0.023188	
$\begin{array}{c} \textbf{C} & -0.872655 & -0.048579 & -0.012732 \\ \textbf{C} & 1.498758 & 0.200579 & -0.121172 \\ \textbf{H} & -0.658520 & -0.731912 & 0.839315 \\ \textbf{H} & -1.419752 & -0.612203 & -0.796487 \\ \textbf{H} & -1.514077 & 0.782782 & 0.345983 \\ \textbf{N} & 0.351223 & 0.500017 & -0.581535 \\ \textbf{O} & 2.615024 & -0.090684 & 0.326629 \\ \textbf{C} & -1.321954 & 0.079847 & -0.059915 \\ \textbf{C} & 0.125140 & 0.194559 & 0.278307 \\ \textbf{H} & -1.848828 & -0.492848 & 0.731931 \\ \textbf{H} & -1.772167 & 1.091808 & -0.134570 \\ \textbf{H} & 0.567039 & 1.175157 & 0.409184 \\ \textbf{H} & 2.659033 & 0.076802 & 0.861245 \\ \textbf{N} & 0.845312 & -0.873562 & 0.413794 \\ \textbf{O} & 2.186822 & -0.810420 & 0.726078 \\ \textbf{C} & 0.023609 & 0.174787 & 0.475047 \\ \textbf{H} & 2.152264 & -0.041841 & 0.244225 \\ \textbf{H} & 1.187776 & -0.518005 & -1.199231 \\ \textbf{Carbamide / Urea} & \textbf{H} & -2.122930 & 0.259006 & 0.346006 \\ \end{array}$		N	1.132081	-0.281427	-0.328214	
$\begin{array}{c} \text{Methyl Isocyanate} \\ (C_2H_3NO) \\ \\ \\ \\ \\ \\ \\ \\ \\ \\ \\ \\ \\ \\ \\ \\ \\ \\ \\$		О	0.324588	0.105691	0.692069	
$\begin{array}{c} \text{Methyl Isocyanate} \\ (C_2H_3NO) \\ \\ \\ \\ \\ \\ \\ \\ \\ \\ \\ \\ \\ \\ \\ \\ \\ \\ \\$		С		-0.048579		
$ \begin{array}{c} \text{Methyl Isocyanate} \\ (C_2H_3NO) \\ \\ H \\ \\ -1.419752 \\ \\ H \\ -1.514077 \\ \\ 0.782782 \\ 0.345983 \\ \\ N \\ 0.351223 \\ 0.500017 \\ -0.581535 \\ O \\ 2.615024 \\ -0.090684 \\ 0.326629 \\ \\ C \\ -1.321954 \\ 0.079847 \\ -0.059915 \\ C \\ 0.125140 \\ 0.194559 \\ 0.278307 \\ \\ H \\ -1.848828 \\ -0.492848 \\ 0.731931 \\ H \\ -1.772167 \\ 1.091808 \\ -0.134570 \\ -0.441345 \\ -1.033016 \\ H \\ 0.567039 \\ 1.175157 \\ 0.409184 \\ H \\ 2.659033 \\ 0.076802 \\ 0.861245 \\ N \\ 0.845312 \\ -0.873562 \\ 0.413794 \\ O \\ 2.186822 \\ -0.810420 \\ 0.726078 \\ \\ C \\ 0.023609 \\ 0.174787 \\ 0.475047 \\ H \\ 2.152264 \\ -0.041841 \\ 0.244225 \\ H \\ 1.187776 \\ -0.518005 \\ -1.199231 \\ Carbamide / Urea \\ \end{array} $						
$ \begin{array}{c} \text{Methyl Isocyanate} \\ (C_2H_3NO) \\ \\ H \\ \\ -1.514077 \\ O.782782 \\ O.345983 \\ O.500017 \\ -0.581535 \\ O \\ 2.615024 \\ -0.090684 \\ O.326629 \\ \\ C \\ -1.321954 \\ O.125140 \\ O.194559 \\ O.278307 \\ O.2441345 \\ O.2441345 \\ O.2441345 \\ O.244345 \\ O.246245 \\ O.2186822 \\ O.810420 \\ O.726078 \\ O.2186825 \\ O.218005 \\ O.259006 \\ O.346006 \\ O.345982 \\ O.259006 \\ O.346006 \\ O.3$		1				
$\begin{array}{c ccccccccccccccccccccccccccccccccccc$						
$\begin{array}{c ccccccccccccccccccccccccccccccccccc$	$(C_2H_3NO)$	Н				
$\begin{array}{c ccccccccccccccccccccccccccccccccccc$		1				
$\begin{array}{c} C \\ C \\ O.125140 \\ O.194559 \\ O.278307 \\ C \\ O.125140 \\ O.194559 \\ O.278307 \\ O.278207 \\ O.2$		О				
$\begin{array}{c ccccccccccccccccccccccccccccccccccc$		С				
$ \begin{array}{cccccccccccccccccccccccccccccccccccc$						
$ \begin{array}{c} \text{Acetaldehyde Oxime} \\ (C_2H_5NO) \\ \end{array} \begin{array}{c} \text{H} \\ \text{H} \\ \end{array} \begin{array}{c} -1.772167 \\ -1.440397 \\ \end{array} \begin{array}{c} -0.441345 \\ -0.441345 \\ \end{array} \begin{array}{c} -1.033016 \\ -1.033016 \\ \end{array} \\ \text{H} \\ \end{array} \begin{array}{c} 0.567039 \\ -0.873562 \\ \end{array} \begin{array}{c} 0.409184 \\ -0.873562 \\ \end{array} \begin{array}{c} 0.861245 \\ \end{array} \\ \text{N} \\ 0.845312 \\ 0.2186822 \\ -0.810420 \\ \end{array} \begin{array}{c} 0.726078 \\ \end{array} \\ \text{C} \\ 0.023609 \\ 0.174787 \\ 0.475047 \\ \end{array} \\ \begin{array}{c} \text{C} \\ 0.023609 \\ \text{H} \\ 1.187776 \\ -0.518005 \\ \end{array} \begin{array}{c} -1.99231 \\ -1.199231 \\ \end{array} \\ \text{Carbamide / Urea} \\ \end{array} $		Н				
Acetaldenyde Oxime $(C_2H_5NO)$ H $-1.440397$ $-0.441345$ $-1.033016$ H $0.567039$ $1.175157$ $0.409184$ H $2.659033$ $0.076802$ $0.861245$ N $0.845312$ $-0.873562$ $0.413794$ O $2.186822$ $-0.810420$ $0.726078$ C $0.023609$ $0.174787$ $0.475047$ H $2.152264$ $-0.041841$ $0.244225$ H $1.187776$ $-0.518005$ $-1.199231$ Carbamide / Urea H $-2.122930$ $0.259006$ $0.346006$		Н				
H 0.567039 1.173137 0.409184 H 2.659033 0.076802 0.861245 N 0.845312 -0.873562 0.413794 O 2.186822 -0.810420 0.726078 C 0.023609 0.174787 0.475047 H 2.152264 -0.041841 0.244225 H 1.187776 -0.518005 -1.199231 Carbamide / Urea H -2.122930 0.259006 0.346006		Н			-1.033016	
N 0.845312 -0.873562 0.413794 O 2.186822 -0.810420 0.726078  C 0.023609 0.174787 0.475047 H 2.152264 -0.041841 0.244225 H 1.187776 -0.518005 -1.199231 Carbamide / Urea H -2.122930 0.259006 0.346006	$(C_2H_5NO)$	Н	0.567039	1.175157	0.409184	
O         2.186822         -0.810420         0.726078           C         0.023609         0.174787         0.475047           H         2.152264         -0.041841         0.244225           H         1.187776         -0.518005         -1.199231           Carbamide / Urea         H         -2.122930         0.259006         0.346006		Н	2.659033	0.076802	0.861245	
C 0.023609 0.174787 0.475047 H 2.152264 -0.041841 0.244225 H 1.187776 -0.518005 -1.199231 Carbamide / Urea H -2.122930 0.259006 0.346006		N	0.845312	-0.873562	0.413794	
H 2.152264 -0.041841 0.244225 H 1.187776 -0.518005 -1.199231 Carbamide / Urea H -2.122930 0.259006 0.346006		О	2.186822	-0.810420	0.726078	
H 1.187776 -0.518005 -1.199231 Carbamide / Urea H -2.122930 0.259006 0.346006		С	0.023609	0.174787	0.475047	
H 1.187776 -0.518005 -1.199231 Carbamide / Urea H -2.122930 0.259006 0.346006		Н	2.152264	-0.041841	0.244225	
Carbamide / Urea H -2.122930 0.259006 0.346006		Н	1.187776			
(CH.N.O) H 1 204020 0 242649 1 120010	Carbamide / Urea	Н	-2.122930			
(C1141V2O)	$(CH_4N_2O)$	Н	-1.304030	-0.342648	-1.139910	
	· /	N	-1.243207		-0.161562	
					-0.220304	
O 0.082288 0.609201 1.655728		1				
N -0.222631 0.458624 0.000000	N' 1011 '1	N				
Nitrosyl Chloride 0 1 157638 0 281711 0 000000						
(NOCI) Cl 1.380269 -0.176914 0.000000	(NOCl)					
					-0.304395	
O = 1.272167 = 0.443194 = 0.630206	TT 1 d'					
Hydroxythiocyanate						
(HOSCN) C 1.126988 -0.244750 0.353656	(HUSCN)					
N 2.142645 0.282231 0.181157						